Nanoscale

Electrochromic thin films of tungsten oxide with high-exposure (002) crystal faces doped and modulated by cerium acetate

Journal:	*Nanoscale*
Manuscript ID	NR-ART-12-2024-005095.R1
Article Type:	Paper
Date Submitted by the Author:	30-Dec-2024
Complete List of Authors:	Nie, Shanshan; Tianjin Chengjian University Wang, Chengyi; Tianjin Chengjian University Zhou, Miao; Tianjin Chengjian University Lian, Li; Tianjin Chengjian University Liu, Jie; Tianjin Urban Planning and Design Institute Co Ltd Ruan, Mengnan; Tianjin Chengjian University Liu, Zhifeng; Tianjin Chengjian University, Materials Science and Engineering

Electrochromic thin films of tungsten oxide with high-exposure (002) crystal faces doped and modulated by cerium acetate

Shanshan Nie[1], Chengyi Wang[1,2], Miao Zhou[1,2], Yi Lian[3], Jie Liu[3], Mengnan Ruan[1,2#], Zhifeng Liu[1,2*]

(1 School of Materials Science and Engineering, Tianjin Chengjian University, 300384, Tianjin, China. 2 Tianjin Key Laboratory of Building Green Functional Materials, Tianjin Chengjian University, 300384, Tianjin, China. 3 Tianjin Urban Planning and Design Institute Co. Ltd., 300000, Tianjin, China.)

Abstract: The electrochromic layer is the key part of the electrochromic device, and it is usually necessary to introduce nanomaterials or other functional materials to improve the response speed and stability. In this paper, a cerium acetate-doped tungsten oxide film (WO_3-CA) prepared by hydrothermal and annealing method is presented and compared with pure tungsten oxide film (WO_3) and acetate-doped tungsten oxide film (WO_3-HAC) in terms of electrochromic performance. The electrochemical analysis results show that the Li^+ diffusion rate of the WO_3-CA film is 37.36×10^{-12} cm^2/s, which is 2.6 and 2.2 times higher than that of pure WO_3 (14.21×10^{-12} cm^2/s) and WO_3-HAC (16.93×10^{-12} cm^2/s), respectively. Combined with density-functional theory (DFT) simulations , it was investigated that the introduction of cerium acetate forms new Ce-O coordination bonds with oxygen atoms in WO_3 and exposes more (002) crystal faces. In addition, the introduction of acetate ions also contributes to the improvement of the structural stability and electrochemical properties of the films, which promotes the enhancement of the electrochromic effect. This mechanism provides a new idea for optimizing electrochromic materials.

Keywords: WO_3; cerium acetate-doped; DFT; (002) crystal faces; electrochromism

1. Introduction

Due to the non-renewability of traditional energy sources such as coal and oil and the environmental pollution they cause, there is a growing global demand for clean energy and energy-saving technologies, which is driving sustainable development and environmental awareness [1-3]. Among these energy sources, smart color-changing devices have gradually become a new type of energy source of concern due to its

corresponding author E-mail: 15101175504@163.com
* corresponding author E-mail: tjulzf@163.com

environmental friendliness and wide range of raw materials [4-7]. Electrochromic technology can adjust the optical properties of materials under various environmental conditions, usually by triggering a reversible redox reaction in the material under the action of an electric field, thus changing its optical performance such as color or transparency. The electronic structure or chemical composition of the material is changed, thus affecting the absorption or reflection of light to achieve energy saving effects [8-10].

Typical electrochromic devices usually consist of multiple components and must meet some key requirements for fast and efficient switching between colored and colorless states [11-13]. By adjusting the light transmission of windows to reduce direct sunlight into the room, the air conditioning load can be reduced and energy can be saved [14]. The application of electrochromic devices in the fields of architecture, automobiles and electronic devices is gaining more and more attention, which helps to achieve the goal of sustainable development [15-17].

WO_3 is a very important metal oxide that has been widely studied for its excellent electrochromic properties [18]. Ma et al. used a simple hydrothermal method to directly grow thin films of WO_3 nanoribbons with different morphologies on FTO glass to selectively synthesize ordered honeycomb structures woven by nanoribbons with a large specific surface area [19]. Yang et al. prepared WO_3 films with electrochromic properties by spin-coating method, able to gradually lose the crystalline water of the product with the increase of heat treatment temperature. And the prepared film has many small cracks, which is conducive to the effective penetration of the electrolyte [20]. However, conventional WO_3 materials are limited in practical applications due to their insufficient light modulation, weak diffusion coefficients and poor coloring efficiency [21-23]. In recent years, researchers have actively explored various methods to enhance their electrochemical properties to overcome these limitations [24-26]. Morankar et al. successfully prepared molybdenum-doped tungsten oxide (W-Mo) electrodes by using the electrodeposition technique. And the 2w% doped WMo-2 films exhibited excellent electrochromic properties, could effectively accommodate Li^+, and showed desirable dual functional properties [27]. Shen et al. introduced Co doped WO_3 films with modified morphology and enhanced electrochromic properties by seedless hydrothermal method. The surface morphology of Co doped WO_3 films was significantly changed and exhibited higher transmittance modulation and better long term stability [28].

For this reason, various heteroatoms such as erbium (Er), lanthanum (La), europium (Eu) and Ce can be attempted to be introduced in WO_3. Among them, Ce, as a rare-earth metal element, has attracted much attention because of its ability to enhance optical, photovoltaic and electrochromic properties when doped or coupled with different oxide semiconductors [29, 30]. Klein et al. modified mesoporous antimony doped tin oxide (ATO) nanoparticle layers with redox active cerium compounds. The cerium modified ATO films were used as electrochromic working electrodes and the 15% Sb doped nanoparticle layer had the highest capacity and high conductivity [31]. Dhanasankar et al. prepared Ce doped molybdenum oxide thin films on FTO coated glass substrates using sol-gel dip coating method at 250 °C. The amorphous structure of this film facilitates the process of embedding and de-embedding of ions, thereby enhancing its electrochromic properties [32]. Therefore, Ce can be chosen as additives for doped WO_3 films, and the strong luminescent properties of Ce enhance the luminescent effect of WO_3, especially in the UV and visible region. This makes doped WO_3 even more promising for display technology and electrochromic devices.

In this study, three types of films were prepared on FTO glass substrates using hydrothermal and annealing techniques: pure WO_3 films, WO_3-HAC films and WO_3-CA films. A comprehensive study of the doped WO_3 films was conducted to explore the effects and advantages of Ce as a dopant. And to gain insight into its influence on the structure, morphology and electrochromic properties of WO_3. Doped Ce will introduce additional electronic states, leading to a change in the electronic energy band structure of the material. This change not only affects the electronic energy levels of the WO_3 material, but also directly influences its conductivity, optical properties, and ability to modulate light transmission. The presence of Ce dopant will form new Ce-O bonds with oxygen atoms in WO_3, affecting the crystal structure and local environment of the material. At the same time, doping Ce exposes more (002) crystal planes and provides more ionic embedding and de-embedding sites, allowing ions (H^+, Li^+) to migrate through the material more easily. Additionally the adsorption of acetate ions in cerium acetate may also have an effect on the properties of WO_3 films. The surface chemical environment of the material is modified by the formation of additional ionic interactions on the surface or inside the film.

2. Experimental section

2.1 Synthesis of pure WO_3 films, WO_3-HAC films and WO_3-CA films

In this synthesis, $Na_2WO_4 \cdot H_2O$ and $K_2C_2O_4$ were used as the main precursors.

First, the two compounds were dissolved in 50 mL of deionized water to ensure their complete dissolution. Then, 3 M hydrochloric acid was slowly added to adjust the pH of the solution (pH 1.2~1.5), thereby promoting the precipitation of tungstate. Next, stirring was continued for 1 to 2.5 h at room temperature to mix the reactants sufficiently to form a white turbid solution. In preparing a sample of WO_3 doped with acetic acid or cerium acetate, the dopant was added to the white precursor while ensuring that the molar ratio of acetic acid remained consistent. Subsequently, the solution was transferred to a Teflon-lined stainless steel autoclave while a cleaned and dried FTO (fluorine doped tin oxide) conductive glass substrate was placed obliquely inside the autoclave. After sealing, the solution was heated in an oven at 180 °C for 6 h. After the temperature was reduced to room temperature, the prepared film was removed and the substrate was rinsed several times with deionized water to remove the residue on the surface. Finally, the films were dried at 60 °C for 30 min and the pure WO_3 films and doped WO_3 films were obtained by adjusting the calcination temperature (550 °C) and time (2 h).

2.2 Characterization

The x-ray diffraction (XRD) of the three prepared films was recorded with Cu Kα radiation (λ = 0.1542 Kα). The morphology and structure of the synthesized products were characterized by in a Philips XL-30 field emission scanning electron microscope and transmission electron microscope (TEM, JEM-2100F, 200 kV), and energy dispersive spectroscopy (EDS) data were collected. Infrared spectra were recorded using Fourier transform infrared spectrometer (FTIR) in the wave number range of 4000-400 cm^{-1} . The relative content of the films and the transmission spectra of the films were studied using X-ray photoelectron spectroscopy (XPS) and UV spectrophotometer, respectively. Cyclic voltammetry (CV), current density-voltage (I-V) and current density-time (I-T) curves of the films were recorded using an electrochemical workstation (CHI760E). A three-electrode system (working electrode, counter electrode and reference electrode; 1.0 $molL^{-1}$ $LiClO_4$ in PC was used as electrolyte) was used [33, 34].

DFT simulations were all performed in Materials Studio 2019 software. The Dmol-3 module hybridization was chosen for structure optimization and energy calculations for the three films and their corresponding embedded Li^+ structures.

3. Results and discussion

3.1. Characteriazation of samples

The synthesis of pure WO_3 films, WO_3-HAC films and WO_3-CA films is illustrated in Fig. 1. Firstly, precursor solutions containing the corresponding dopants were prepared using FTO glass as a substrate. Next, a hydrothermal method was used to promote the uniform growth of the films and ensure the homogeneity of the materials. Finally, the crystallinity of the films was improved by annealing treatment to enhance the electrochromic properties of the films.

Compared the SEM images of pure WO_3 s (Fig. 2a), WO_3-HAC (Fig. 2b) and WO_3-CA (Fig. 2c) nanostructures, a wide range of WO_3 films with various morphologies were synthesized by varying the dopants in the precursor solution while keeping the growth environment unchanged on the substrate. The undoped WO_3 rod-like structures are up to 2 μm long and have a relatively uniform and regular structure. At the doping level of W:AC=1:3, the length of the nanorods became shorter and showed the structure of wheat ears, this change in structure may be due to the acetic acid changing the direction or rate of growth of the nanorods. At the same time, the acetic acid molecules may have affected the decomposition process of the precursors or the self-assembly of the nanorods, resulting in a looser film layer. When Ce was introduced (W:AC:Ce=1:3:1), the nanorod morphology produced nanorods with more voids and larger contact areas compared to the acetic acid-modulated nanorod morphology. The doping of Ce may have affected the crystallization process of WO_3 and changed the lattice structure of WO_3, resulting in more holes during film growth. Meanwhile, acetic acid acts as a ligand in this system, which helps to stabilize the precursors of Ce and tungsten improving the dispersion and homogeneity of the materials.

HR-TEM images confirm that the lattice spacing of pure WO_3 nanorods (Fig. S1) is about 0.365 nm, corresponding to the value of the (200) plane. This is consistent with the growth of nanorods along the <200> direction in a monoclinic structure. A slight change (increase of 3.4%) in the lattice spacing (020) of the acetate-doped nanorods is observed from Fig. 2d and Fig. 2 for the pure WO_3 nanorods. The increased lattice spacing may have reduced the effect of lattice defects and improved the free mobility of electrons, and the change suggests that acetic acid may have been successfully embedded in the crystal structure.

The (002) plane is a crystalline plane with high surface energy and high reactivity. Doping Ce ions on top of acetic acid exposes more (002) planes to regulate the growth direction and surface structure of the material and can increase the surface active sites

to improve the electrochromic properties. Due to the relative orientation between the (200) and (010) planes, it can help to determine the relative alignment of the nanorods. And the overlapping features of the nanorods may lead to changes in the charge transport paths, affecting the electrical conductivity of the material and the electrochromic reaction rate. The TEM observations (Fig. 2e and g) show agreement with the results of the (002) peak in the XRD results in Fig. 3a.

In the XRD patterns of undoped and doped samples (Fig. 3a), it was observed that the characteristic peaks of FTO substrate were detected in all the samples in accordance with JPCDS No. 77-0452. These peaks correspond to the characteristic diffraction peaks of FTO, indicating that the substrate is consistent in the XRD pattern. The XRD pattern of pure WO_3 corresponds to JPCDS No. 43-1035, which confirms the main base crystal feature of its monoclinic phase [35]. And the three main diffraction peaks at about 23.12°, 23.58° and 24.38° (2θ) can be assigned to (002) (020) and (200), respectively. For doped acetate samples, the XRD patterns will show small intensity changes in the peak positions. These changes can reflect the effect of doping on the crystal structure. The full width at half maximum (FWHM) of the (020) plane and the (200) plane exhibit larger values, corresponding to smaller sized nanostructures. This result is in good agreement with the SEM observations (Fig. 2b) (the structure becomes shorter and wider under the dopant of acetic acid). However, immediately after Ce doping, the (002) plane has the highest diffraction intensity, indicating that this crystalline plane has preferential stacking or orientation in the sample. This phenomenon usually indicates that the plane occupies a predominantly oriented position in the sample, implying that the crystals of the sample are aligned predominantly along the <002> direction. Preferential orientation of the (002) plane indicates that the plane is oriented in the same direction as the long axis of the nanorod. It indicates that the nanorod has a significant crystal orientation along a specific direction (the axial direction of the nanorod) during the growth process. From the XRD results, no stronger evidence of a change in crystal structure between the doped and undoped samples was found. The EDS pattern shows characteristic peaks of the elements in the sample. By identifying these characteristic peaks, it is possible to determine the presence of the element Ce in the sample and its relative content. The stoichiometric ratios of the relative atomic ratios of the products prepared from the three samples are shown in Tab. S1 as well as the corresponding W, O, C, and Ce contents (Fig. 3c and Fig. S3) [36].

The infrared spectra in the range of 4000-400 cm^{-1} were utilized to analyze and characterize three substances, pure WO_3, WO_3-HAC and WO_3-CA (Fig. 3b). Firstly, a distinct absorption peak appeared at about 1120 cm^{-1}, which is usually associated with the W=O related telescopic vibrational mode, one of the typical vibrational features in WO_3. Moreover, the absorption peak observed at 795 cm^{-1} may be associated with the O-W-O bending vibrational mode in WO_3 films. And the absorption band at 669 cm^{-1} is correlated with the Ce-O stretching vibrational mode, suggesting that the doping of Ce may introduce new vibrational modes by forming new chemical bonds with the WO_3 surface. In particular, the absorption peak observed at 2360 cm^{-1} may be related to the introduction of new chemical species (-OH, -COOH) by acetic acid or cerium acetate, which in turn affects the vibrational modes of the surface functional groups. The results show that some of the peaks of WO_3-CA films are higher compared to pure WO_3 films. Specifically, these enhanced peaks may be due to the formation of new chemical bonds between the dopant and the WO_3 surface, changing the local structure of the material or introducing new vibrational modes [37, 38].

The chemical compositions of the three samples were examined using XPS, and the results are shown in Fig. 4(d)-(f). The XPS analysis shows that the 4f energy level of W is manifested in the spectra as two major peaks, W $4f_{5/2}$ at 37.88 eV and W $4f_{7/2}$ at 35.75 eV, respectively. The two peaks correspond to the spin orbitals of W, indicating that W in the sample mainly exists in the W^{6+} oxidation state. With the doping of acetic acid, the W 4f peak shifted to a lower binding energy, indicating that the tungsten atoms underwent a reduction process and the oxidation state of W decreased, changing the chemical state of W. A lower oxidation state typically indicates a higher electron density on the tungsten atoms, which can influence the material's conductivity and electrochromic properties. The addition of Ce ions immediately afterward resulted in a slight shift of the W 4f peaks. This change in peak position may reflect the interaction between W and Ce ions and has a subtle effect on the local chemical environment of W, ultimately affecting the electronic properties and structural stability of the material [39, 40].

The O 1s spectrum shows two main peaks. Two peaks at 530.53 eV and 531.70 eV were present in pure WO_3, which gradually increased in intensity with the addition of dopant. The dopant may add hydroxide or water molecules by changing the surface chemical state of the material. This leads to the rearrangement of oxygen atoms and enhances the intensity of the relevant peaks in the O 1s spectrum. Cerium doping alters

the chemical environment of oxygen by forming new Ce-O coordination bonds, resulting in a change in the oxygen binding state. It may also increase the proportion of hydroxide or surface adsorbed water molecules, thus affecting the peak position and intensity of the O 1s spectra [41].

In Ce-doped samples, the oxidation state and ionic radius of Ce have a significant effect on the doping process. The binding energy values of Ce^{3+} and Ce^{4+} are 885.98 eV and 904.17 eV (Ce^{3+} $3d_{5/2}$ and $3d_{3/2}$), and 882.11 eV and 900.12 eV (Ce^{4+} $3d_{5/2}$ and $3d_{3/2}$), respectively. It is difficult to effectively replace W^{6+} in WO_3 (0.065 nm for W^{6+}) due to Ce ions with their large ionic radii (0.101 nm for Ce^{4+} and 0.103 nm for Ce^{3+}). However, Ce^{3+} can exist in WO_3 in doped form and form new Ce-O bonds with oxygen atoms. The formation of Ce-O bonds leads to local structural changes, lattice distortions, and modifications in the electronic structure. These changes impact the band gap, electrical conductivity, optical properties of WO_3, and its redox behavior, ultimately enhancing its electrochromic performance [42].

3.2. Electrochromic mechanism

WO_3 as an electrochromic film undergoes a typical reversible color change from blue (colored) to transparent (bleached) in the presence of an applied electric field. This process involves a redox reaction in which the W^{6+} in WO_3 are reduced to a lower valence state (W^{5+}). This can be represented by the following equation (1) [43]:

$$WO_3 + xLi^+ + xe^- \rightleftharpoons Li_xWO_3 \quad (1)$$

The mechanism of action of cerium acetate doped WO_3 films is illustrated in Fig. 5. The doping of Ce will form new Ce-O coordination bonds with oxygen atoms in WO_3, and this new chemical environment can affect the electrochromic properties of the films. The formation of Ce-O bonds not only enhances the structural stability of the films, but also may improve the electron and ion conductivity. Meanwhile, the addition of Ce can adsorb acetate ions (CH_3COO^-), which will further change the surface chemistry of the films. The presence of acetate promotes the migration of ions and contributes to the embedding and delocalization of ions required in the electrochromic process. In addition, doping Ce leads to an increased exposure of the (002) crystalline facet in WO_3 films. This crystalline facet plays a key role in the electrochromic performance, as its increased active sites in the film help to increase the diffusion rate of ions, thus speeding up the response time of the color change.

The three film structures (Fig. 6a) of WO_3, WO_3-HAC, WO_3-CA and the charge density distributions in Li^+ electrolyte (Fig. 6b) have been calculated by using the DFT

model. The effects of different doping on the crystal structure of WO_3 films are illustrated and further revealed the differences in charge transfer and ion adsorption after doping. Fig. 6c, Fig. 6d, and Fig. S4 demonstrate the partial density of states (PDOS) of O 2p, W 5d, and Ce 4f orbitals in WO_3,WO_3-CA, and WO_3-HAC films, respectively. These plots show the orbital overlap after Ce doping, especially the effect of Ce 4f orbitals on the overall electronic structure. The increase in the density of the O 2p orbitals can be seen from the figure, which is most likely due to the change in the electron cloud of the oxygen atom due to the formation of the Ce-O bond. At the same time, Ce, as an element with strong oxygen affinity, can accept electrons and form chemical bonds with oxygen atoms. This in turn affects the electron density of the 2p orbitals of the oxygen atom, thus changing the electrical and optical properties of the films. In addition, Fig. 6e shows the total PDOS plots for the three films, summarizing the contributions of all orbitals and providing information on the overall electronic structure of the three films.

3.3. Electrochemical characterization

Cyclic Voltammetry is an effective electrochemical analytical technique for studying chemical processes in thin film samples. In CV experiments, the potential of the working electrode is varied linearly between two set potential limits while maintaining a fixed scan rate (100 mV/s). The peak current can be obtained by measuring the relationship between current and potential. It can be concluded from Fig. 6a that the WO_3-CA film has a higher peak current in the voltage range of -1.5 V-1.0 V. This indicates its better electronic and ionic conductivity and higher electrochemical activity in electrochemical reactions. In addition, by integrating the area under the voltammetric curve, the value of the charge-voltage (Q-V) curve can be obtained (see the Supplemental Information for the formulae in detail), which in turn quantifies the ion storage capacity of the films [44]. The area of the voltammogram is largest under the doping of CA, which reflects the energy storage capacity and electrochromic properties of the material. It can be attributed to the doping of Ce to form a new Ce-O coordination bond, which facilitates the migration of ions, making the electrochemical reaction more efficient and enhancing the conductivity of the film. It also leads to a fuller exposure of the (002) crystal surface, which increases the active sites and thus improves the reactivity of electrochromism. Moreover, the adsorption of acetate ions optimizes the kinetics of the electrochemical reaction and accelerates the reaction rate.

The effective diffusion coefficients of Li^+ (D_{Li^+}) were calculated according to the

Randles-Sevcik equation (see the Supplemental Information), which is commonly used to analyze the kinetics and diffusion behavior of electrochemical reactions (assuming that this is a simple solid-state diffusion-controlled process) [45]. Fig. S6d-f show the variation of currents for the three films at different scanning speeds. It can be concluded that $D(WO_3)=14.21\times10^{-12}$ cm^2/s, $D(WO_3\text{-HAC})=16.93\times10^{-12}$ cm^2/s and $D(WO_3\text{-CA})=37.36\times10^{-12}$ cm^2/s. The Li^+ diffusion coefficient of WO_3-CA is about 2.6 times higher than that of the pure WO_3, which suggests that CA doping significantly enhances the Li^+ mobility and improved electrochemical performance. The introduction of CA may have improved the microstructure of the WO_3 films by increasing the number and permeability of ion channels, enabling smoother migration of Li^+. The doped Ce were able to optimize the diffusion path of Li^+ and reduced the migration barrier of Li^+ in the electrode materials, which led to faster Li^+ embedding and de-embedding processes.

Electrochemical impedance spectroscopy (EIS) of the three films can demonstrate their electrochemical properties (Fig. 6b). Typically, these curves exhibit different semicircles (high-frequency region) and slopes (low-frequency region) reflecting their respective charge transfer impedance and diffusion behaviors at a voltage of 0 V. The WO_3-CA film has smaller semicircle diameters showing smaller impedance values and lower straight line slopes indicating faster Li^+ migration and higher reaction rates [46]. Based on the resistance values fitted from the electrochemical impedance spectroscopy equivalent circuit, the WO_3-CA composite material exhibits excellent electrochemical performance. Its solution resistance (R_1) is 9.33 Ω, and its charge transfer resistance (R_2) is 33.21 Ω, indicating low conductivity and good charge transfer capability, which facilitates fast-response electrochromic characteristics. In contrast, WO_3-HAC has a solution resistance of 38.72 Ω and a charge transfer resistance of 52.33 Ω, suggesting certain barriers in current conduction and charge transfer. WO_3 has a solution resistance of 61.38 Ω and a charge transfer resistance of 52.45 Ω, with overall electrochemical performance being inferior to both WO_3-CA and WO_3-HAC. Therefore, the WO_3-CA composite material outperforms pure WO_3 and WO_3-HAC in electrochromic performance, particularly in improving response speed and stability [47]. The doping of CA enhanced the electrical conductivity of the material through the formation of Ce-O coordination bonds. This coordination not only reduces the charge transfer impedance, but also optimizes the electronic and ionic conductivity of the electrode, making the electrochemical reaction more efficient. Meanwhile the exposure of more (002) crystalline surfaces improves the interfacial properties between the electrode and

the electrolyte and enhances the interfacial reaction rate.

Different dopants lead to changes in the I-V curves, thus reflecting the effect of doping on the conductivity properties. Fig. 6c illustrates the I-V curves of the three films. In the voltage range of -1.5 V to 1.0 V, the WO_3-CA film curves exhibit larger slopes compared to the other films. The large slope implies that the WO_3-CA films are able to transfer the current more efficiently and show higher electrical conductivity. The doping of CA may have increased the carrier concentration or improved the carrier mobility, leading to a more sensitive current response. Furthermore, doping Ce enhanced the adsorption of acetate ions, leading to a further increase in the number of charge carriers.

The I-T curves of the three films illustrated in Fig. S5 can reveal their current response characteristics at different times, and the trend of current over time can reflect the stability of each film. By analyzing the curves, the WO_3-CA film flattens out earlier, a property that reflects its good electrochemical stability. It means that it can adapt quickly and maintain a high current density when the external conditions change. The high current density means that the films have good electrical conductivity and carriers are able to move quickly through the material, reducing resistive losses. It is attributed to the formation of Ce-O coordination bonds between cerium and oxygen atoms of coordination bonds that enhance the structural stability of the material. This strong coordination helps stabilize the charge carriers, making it easier for electricity to flow in the presence of an electric field.

The difference in open-circuit potential (OCP) indicates the effectiveness of different films in carrier separation and transport, and Fig. 6d demonstrates the open-circuit voltages of the three films. The results show that the WO_3-CA film not only has a higher open-circuit voltage, but also exhibits a smoother trend. This implies that the film is not only stable in the electrochemical environment, but also able to maintain its performance for a longer time. This suggests that Ce doping enhances both the electronic and ionic conductivity of the film, facilitating carrier migration. And the adsorption of acetate increases surface reactivity, thereby contributing to an improved electrochemical reaction rate. In addition, the incorporation of Ce optimizes the structure of the films, reduces the instability in the electrochemical reaction and enhances the durability.

The Cdl (double-layer capacitance) curves of these three films (Fig. 7d) were analyzed to understand the charge storage capacity and reactivity of different films in

electrochemical reactions. The CV tests at different scan rates were carried out with the open-circuit voltage as the center potential (Fig. S6a-c), taking ±50 mV potential intervals and calculating the Cdl values based on the scan rates. It can be seen that the larger slope of the WO_3-CA film reflects the faster charge transfer process, and the film is able to effectively promote the transfer of electrons and enhance the reaction kinetics. Meanwhile the higher Cdl values may indicate that the films have more active sites due to more exposure of the (002) crystal surface, which helps to enhance the electrochemical reaction. In addition, a stable Cdl profile tends to imply that the films exhibit good durability and consistency in electrochemical reactions [48].

Response time curves in electrochemical reaction tests are commonly used to evaluate the dynamic characteristics and performance of electrochemical systems. Fig. 7a-c shows the response time curves of three thin films at voltages from -1.5 V to 1.5 V. The curves reflect the dynamic process of color change of the electrochemical system after the application of voltage. And the slope of the curves can indicate the charge transfer capability at the electrode interface, the steeper the slope, the more rapid the charge transfer. The color transition of WO_3-CA films was shown to occur within 2.1 s by the intercept with the plane. And the current density reached equilibrium after 13.4 s, indicating that the process of color change of the films was completed. This indicates that Ce doping enhances coloring efficiency by influencing the conductivity and ion mobility of the oxide through the formation of new Ce-O bonds. Additionally, the adsorption of acetic acid molecules improves the reaction kinetics of the electrode.

3.4. Characterization of optical properties

In electrochromic materials, the change of transmittance directly reflects the optical properties of the material in different states. Regarding the transmittance of the three films in Fig. 8a-d between 300 nm and 800 nm in the colored and faded states as well as the color display plots to compare their optical properties. By comparing the depth of coloration and the range of optical modulation (ΔT) of the different films at λ = 600 nm (see Supplemental Information for the equations). The WO_3-CA film has a larger ΔT of 51.99%, which is 1.65 times that of the pure WO_3 film. The reason for exhibiting this property may be due to the introduction of Ce contributing to more efficient ion migration. This allows the films to respond more rapidly to electrochemical processes, resulting in enhanced light modulation. Doping of Ce improves its ionic conductivity and optical properties, while optimization of the electronic structure leads to higher light absorption and reflection properties. Therefore, further adsorption of

acetate enhances the light-film interaction and improves the light modulation range. Compared to other reported works, WO_3-CA exhibits outstanding electrochromic performance (Table S4). In addition to having the highest transmittance change (52.0% & 600 nm), which is similar to that of previously reported materials, it also has the shortest coloring and bleaching times (2.1 seconds), demonstrating extremely fast response and recovery capabilities.

The coloration efficiency (CE) is an important metric for evaluating the performance of electrochromic materials in specific applications (smart windows, displays). A higher coloration efficiency means that the material is able to produce a more pronounced color change for the same electrical charge. This can be calculated using the formula provided in the Supplemental Information. The calculation gives CE(WO_3)=60.33 cm^2/C, CE(WO_3-HAC)=75.66 cm^2/C, CE(WO_3-CA)=112.14 cm^2/C. The results show that the WO_3-CA film has a higher coloring efficiency, implying that the material forms new Ce-O bonds due to doping by the rare-earth element cerium, which may lead to a higher ion mobility and more efficient charge injection or extraction. Moreover, the interaction of acetate ions with the interface of WO_3-CA films can improve the interfacial properties of the electrolyte and the electrodes. It improves the electrochemical reaction rate of the electrode and further enhances the coloring efficiency.

4. Conclusion

Herein, WO_3 films, WO_3-HAC films, and WO_3-CA films were successfully prepared via hydrothermal and annealing methods. During the doping process, the molar ratio of acetic acid to cerium was maintained at 3:1 to ensure a fixed doping ratio of cerium. X-ray diffraction analysis revealed that the cerium-doped WO_3 films exhibited a more prominent diffraction peak at the (002) crystal plane, indicating that the crystal growth process was more orderly, with improved crystal orientation and crystallinity. Electrochemical testing results showed that the electrochromic performance of the WO_3-CA film was significantly superior to that of the pure WO_3 film. Specifically, at a scanning rate of 100 mV/s, the lithium ion diffusion coefficient of the WO_3-CA film was 37.36×10^{-12} cm^2/s, much higher than the 14.21×10^{-12} cm^2/s of the pure WO_3 film, indicating smoother lithium ion migration after cerium doping. The coloration and bleaching response times of the WO_3-CA film were 2.1 seconds, showing rapid reaction; its optical contrast was 51.99%, and the maximum coloration efficiency was 112.14 cm^2/C, demonstrating excellent optical modulation performance.

The improvement in electrochromic performance can be attributed to several factors: First, the cerium-doped WO_3 films exposed more (002) crystal planes, providing more active sites that helped enhance electrochromic performance. Second, cerium formed new Ce-O coordination bonds with oxygen atoms in WO_3, which not only improved the chemical stability and optical properties of the material but also optimized the energy transfer and charge distribution during the electrochromic process, accelerating the reaction rate. Finally, the cerium-doped WO_3 films could effectively adsorb acetate ions, promoting ion migration during the electrochromic process and further accelerating the electrochromic reaction.

Acknowledgments

The authors gratefully acknowledge financial support from Key Research and Development Plan of Tianjin (No. 22YFZCSN00010) and National Natural Science Foundation of China (No. 52272009).

References:

[1] Wang J L, Sheng S Z, He Z, et al. Self-powered flexible electrochromic smart window. Nano Letters, 2021, 21: 9976-9982.

[2] Bai T, Li W, Fu G, et al. Dual-band electrochromic smart windows towards building energy conservation. Solar Energy Materials and Solar Cells, 2023, 256: 112320.

[3] Chen M, Zhang X, Sun W, et al. A dual-responsive smart window based on inorganic all-solid-state electro-and photochromic device. Nano Energy, 2024, 123: 109352.

[4] Sheng S Z, Wang J L, Zhao B, et al. Nanowire-based smart windows combining electro-and thermochromics for dynamic regulation of solar radiation. Nature Communications, 2023, 14: 3231.

[5] Liang Y, Cao S, Guo J, et al. Dual-band electrochromic smart window based on single-component nanocrystals. ACS Applied Electronic Materials, 2022, 4: 5109-5118.

[6] Sun F, Cai J, Wu H, et al. Novel extended viologen derivatives for photochromic and electrochromic dual-response smart windows. Solar Energy Materials and Solar Cells, 2023, 260: 112496.

[7] Kim Y, Han M, Kim J, et al. Electrochromic capacitive windows based on all conjugated polymers for a dual function smart window. Energy & Environmental Science, 2018, 11: 2124-2133.

[8] Granqvist C G, Arvizu M A, Qu H Y, et al. Advances in electrochromic device technology: Multiple roads towards superior durability. Surface and Coatings Technology, 2019, 357: 619-625.
[9] Xu T, Walter E C, Agrawal A, et al. High-contrast and fast electrochromic switching enabled by plasmonics. Nature Communications, 2016, 7: 10479.
[10] Wang Q, Cao S, Meng Q, et al. Robust and stable dual-band electrochromic smart window with multicolor tunability. Materials Horizons, 2023, 10: 960-966.
[11] Li F W, Yen T C, Liou G S. Synthesis of high-performance electrochromic material for facile fabrication of truly black electrochromic devices. Electrochimica Acta, 2021, 367: 137474.
[12] Nejad M A F, Ranjbar S, Parolo C, et al. Electrochromism: an emerging and promising approach in (bio) sensing technology. Materials Today, 2021, 50: 476-498.
[13] Wang M, Xing X, Perepichka I F, et al. Electrochromic smart windows can achieve an absolute private state through thermochromically engineered electrolyte. Advanced Energy Materials, 2019, 9: 1900433.
[14] Deng B, Zhu Y, Wang X, et al. An ultrafast, energy-efficient electrochromic and thermochromic device for smart windows. Advanced Materials, 2023, 35: 2302685.
[15] Ghosh T, Kandpal S, Rani C, et al. Recipe for fabricating optimized solid-state electrochromic devices and its know-how: challenges and future. Advanced Optical Materials, 2023, 11: 2203126.
[16] Wang T, Zhang W, Li T, et al. Electrochromic smart window based on transition-metal phthalocyanine derivatives. Inorganic Chemistry, 2024, 63: 3181-3190.
[17] Roy S, Halder S, Chakraborty C. Dimensional perspectives on metal center associated electrochromism in metal-organic coordinated hybrid polymers: unveiling electrochromic dynamics. Coordination Chemistry Reviews, 2024, 519: 216088.
[18] Fortunato J, Zydlewski B Z, Lei M, et al. Dual-band electrochromism in hydrous tungsten oxide. ACS Photonics, 2023, 10: 3409-3418.
[19] Ma D, Li T, Xu Z, et al. Electrochromic devices based on tungsten oxide films with honeycomb-like nanostructures and nanoribbons array. Solar Energy Materials and Solar Cells, 2018, 177: 51-56.
[20] Yang M, Wang J, Zhang S, et al. Synthesis of tungsten oxide films at low processing temperature and their electrochromic properties. Solid State Sciences, 2022, 132: 106990.
[21] Chithambararaj A, Nandigana P, Kumar M K, et al. Enhanced electrochromism

from non-stoichiometric electrodeposited tungsten oxide thin films. Applied Surface Science, 2022, 582: 152424.
[22] Xu J, Li X, Zhang Y, et al. Effect of in situ heating on the growth and electrochromic properties of tungsten trioxide thin films. Materials, 2024, 17: 2214.
[23] Han Z, Tong M, Zhang C, et al. Unlocking dual-band electrochromism with stacked structure of amorphous tungsten oxide and prussian blue. Solar Energy Materials and Solar Cells, 2024, 273: 112939.
[24] Zhang Z, Mo H, Li R, et al. The counterbalancing role of oxygen vacancy between the electrochromic properties and the trapping effect passivation for amorphous tungsten oxide films. Small Science, 2024, 4: 2300219.
[25] Najafi-Ashtiani H, Bilek M M, Akhavan B. Tungsten oxide thin films for electrochromic applications: pulse width-controlled deposition by high-power impulse magnetron sputtering. Advanced Engineering Materials, 2024, 26: 2301378.
[26] Ma W Y, Sung Y M, Chang C T, et al. The preparation of low-cost tungsten oxide films by solution-coating technique and NIR annealing for high-performance complementary electrochromic devices. Optical Materials, 2024, 156: 115990.
[27] Morankar P J, Amate R U, Teli A M, et al. Nanogranular advancements in molybdenum-doped tungsten oxide for superior electrochromic energy storage. Journal of Energy Storage, 2024, 84: 110978.
[28] Shen K, Sheng K, Wang Z, et al. Cobalt ions doped tungsten oxide nanowires achieved vertically aligned nanostructure with enhanced electrochromic properties. Applied Surface Science, 2020, 501: 144003.
[29] Xiong S, Liang D. Effect of Eu Content on Microstructure and Luminescence Properties of WO_3 Nanoparticles. JOM, 2023, 75: 859-871.
[30] Xu L, Gu D, Chang X, et al. Rare-earth-doped tungsten oxide microspheres with highly enhanced photocatalytic activites. Ceramics International, 2017, 43: 10263-10269.
[31] Klein J, Alarslan F, Steinhart M, et al. Cerium-modified mesoporous antimony doped tin oxide as intercalation-free charge storage layers for electrochromic devices. Advanced Functional Materials, 2023, 33: 2210167.
[32] Dhanasankar M, Purushothaman K K, Muralidharan G. Enhanced electrochromism in cerium doped molybdenum oxide thin films. Materials Research Bulletin, 2010, 45: 1969-1972.
[33] Saju S K, Puthirath A B, Wang S, et al. Thermochromic polymer blends. Joule,

2024, 8: 2696-2714.

[34] VS G K, Ganesha M K, Hakkeem H, et al. Ultrathin sputtered NiO films for enhanced electrochromic performance in smart windows. Journal of Materials Chemistry A, 2024, 12: 19378-19391.

[35] Gao J, He D, Zhang J, et al. In-situ growth of porous rod-like tungsten oxide for electrochemical determination of cupric ion. Analytica Chimica Acta, 2023, 1276: 341645.

[36] Kunyapat T, Xu F, Neate N, et al. Ce-Doped bundled ultrafine diameter tungsten oxide nanowires with enhanced electrochromic performance. Nanoscale, 2018, 10: 4718-4726.

[37] Reddy G V A, Abdul Sattar S, Kumar K N, et al. Effect of growth fluid concentration on characteristics of CeO_2 nanorods and WO_3/CeO_2 nanostructured hybrid films for electrochromic applications. Journal of Materials Science: Materials in Electronics, 2023, 34: 1475.

[38] Ashok Reddy G V, Kumar K N, Sattar S A, et al. Structural, optical, and electrochromic properties of rare earth material (CeO_2)/transitional metal oxide (WO_3) thin film composite structure for electrochromic applications. Ionics, 2023, 29: 3731-3742.

[39] Hasani A, Le Q V, Tekalgne M, et al. Tungsten trioxide doped with CdSe quantum dots for smart windows. ACS applied materials & interfaces, 2018, 10: 43785-43791.

[40] Zhou Q S, Chen Y K, Li X B, et al. Preparation and electrochromism of pyrochlore-type tungsten oxide film. Rare Metals, 2018, 37: 604-612.

[41] Rakhi C, Preetha K C. Thermal treatment effects on tungsten oxide nanostructures synthesized by hydrothermal method. Applied Physics A, 2022, 128: 1064.

[42] Sun D H, Zhang J L. Simulated calculation of surface acid-base equilibrium constants and surface species distribution of the nanoceria suspension. Applied Surface Science, 2019, 495: 143563.

[43] Liu H, Zhang Y, Lei P, et al. Selective electrochromic regulation for near-infrared and visible light via porous tungsten oxide films with core/shell architecture. ACS Applied Materials & Interfaces, 2023, 15: 23412-23420.

[44] Sahu D R, Hung C Y, Wang S C, et al. Existence of electrochromic reversibility at the 1000th cyclic voltammetry for spin coating WO_3 film. Ionics, 2017, 23: 3227-3233.

[45] Ortiz J, Acosta D, Magaña C. Long-term cycling and stability of crystalline WO_3

electrochromic thin films prepared by spray pyrolysis. Journal of Solid State Electrochemistry, 2022, 26: 1667-1676.

[46] Zhi M, Huang W, Shi Q, et al. Enhanced electrochromic performance of mesoporous titanium dioxide/reduced graphene oxide nanocomposite film prepared by electrophoresis deposition. Journal of The Electrochemical Society, 2018, 165: H804.

[47] Lu C H, Hon M H, Leu I C. Direct growth of crystalline tungsten oxide nanorod arrays by a hydrothermal process and their electrochromic properties. Journal of Electronic Materials, 2017, 46: 2080-2084.

[48] Pehlivan E, Granqvist C G, Niklasson G A. Impedance spectroscopy of electrochromic hydrous tungsten oxide films. Electronic Materials, 2021, 2: 312-323.

List of Figures:

Fig.1 Schematic diagrams of the preparation process and the corresponding crystal structures of pure WO_3 films, WO_3-HAC films and WO_3-CA films.

Fig.2 SEM images of (a) WO_3, (b) WO_3-HAC, (c) WO_3-CA. TEM imag es and corresponding EDS elemental mapping images of (d) WO_3-HAC and (e) WO_3-CA. TEM images of (f) WO_3 and (g) WO_3-CA with HRTEM images of the corresponding dashed box regions.

Fig. 3 (a) XRD patterns and (b) FTIR spectrum of WO_3, WO_3-HAC and WO_3-CA films. (c) EDS of W, C, O and Ce in WO_3-CA film. High-resolution (d) W 4f, (e) O 1s and (f) Ce 3d XPS spectra of WO_3, WO_3-HAC and WO_3-CA films.

Fig. 4 Schematic diagram of the comparison mechanism between pure WO_3 films and WO_3-CA films on specific crystalline surfaces.

Fig. 5 (a) Computational modeling of WO_3, WO_3-HAC, and WO_3-CA and (b) corresponding charge density differences (the red and blue regions represent the accumulation and dissipation of electron density, respectively). PDOS patterns of O 2p ,W 5d and Ce 4f orbitals for (c) WO_3 and (d) WO_3-CA. (e) PDOS patterns of WO_3, WO_3-HAC and WO_3-CA.

Fig. 6 WO_3, WO_3-HAC and WO_3-CA films with (a) CV curves at a scan rate of 100 mV/s, (b) EIS Nyquist plots at 0 V (V vs. Ag/AgCl), (c) I-V curves and (d) OCP curves.

Fig. 7 Chronoamperometry measurements of (a) WO_3, (b) WO_3-HAC and (c) WO_3-CA films with a square wave potential between -1.5 V and 1.5 V (V vs. Ag/AgCl). (d) Cdl plots of WO_3, WO_3-HAC and WO_3-CA films.

Fig. 8 Optical transmission spectra of (a) WO_3, (b) WO_3-HAC and (c) WO_3-CA films in the colored and bleached states in the range of 300 to 800 nm, and (d) corresponding color contrast plots.

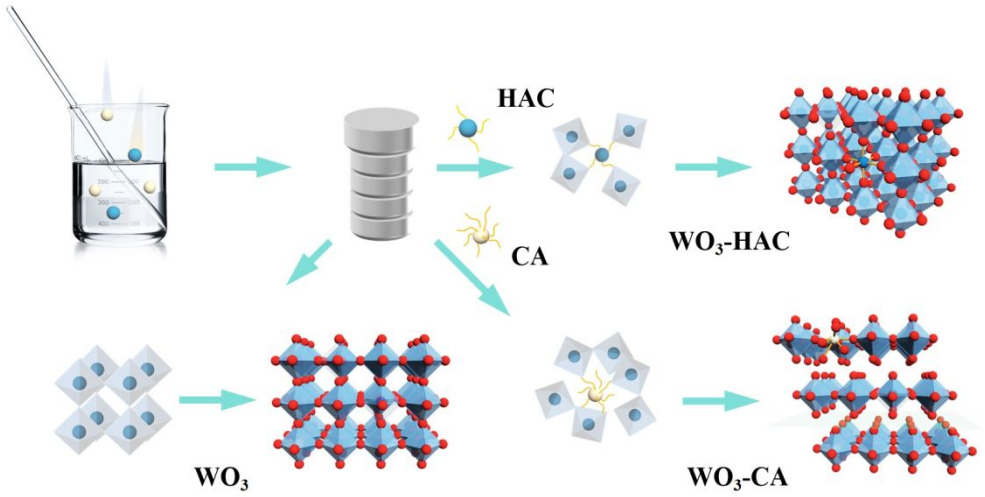

Fig.1 Schematic diagrams of the preparation process and the corresponding crystal structures of pure WO_3 films, WO_3-HAC films and WO_3-CA films.

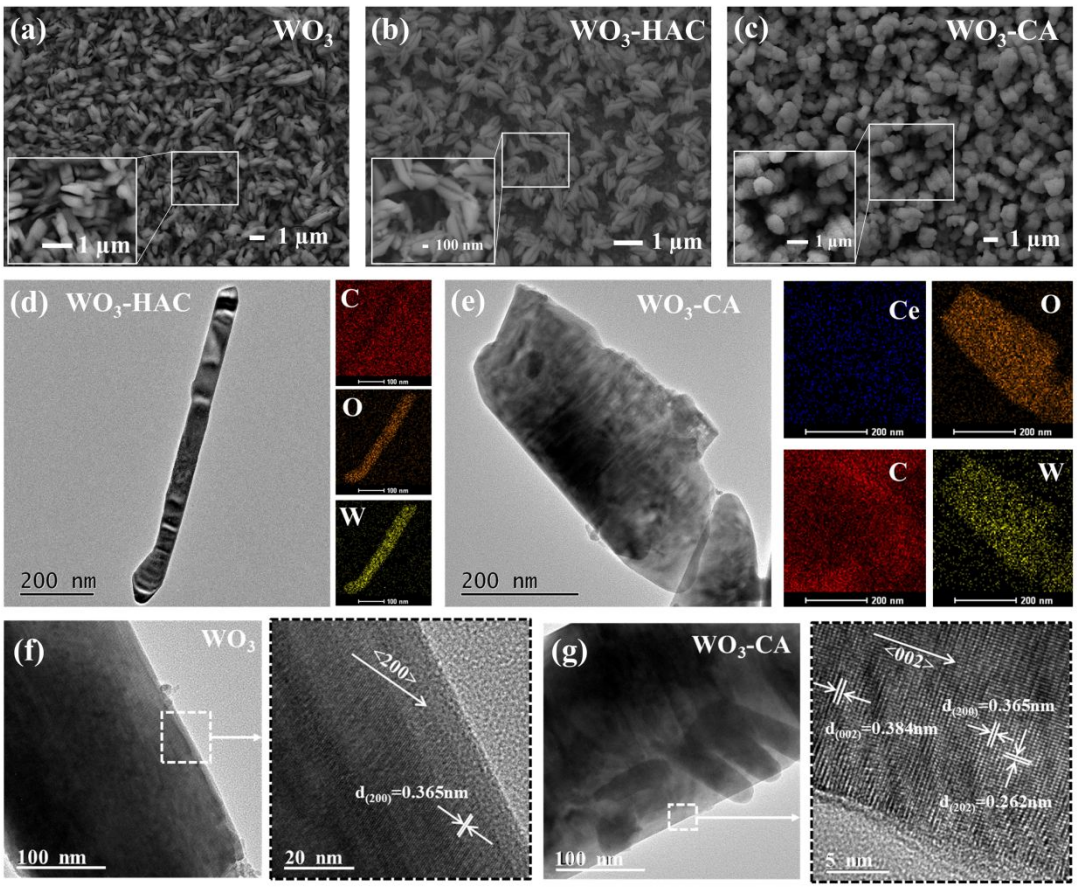

Fig.2 SEM images of (a) WO_3, (b) WO_3-HAC, (c) WO_3-CA. TEM images and corresponding EDS elemental mapping images of (d) WO_3-HAC and (e) WO_3-CA. TEM images of (f) WO_3 and (g) WO_3-CA with HRTEM images of the corresponding dashed box regions.

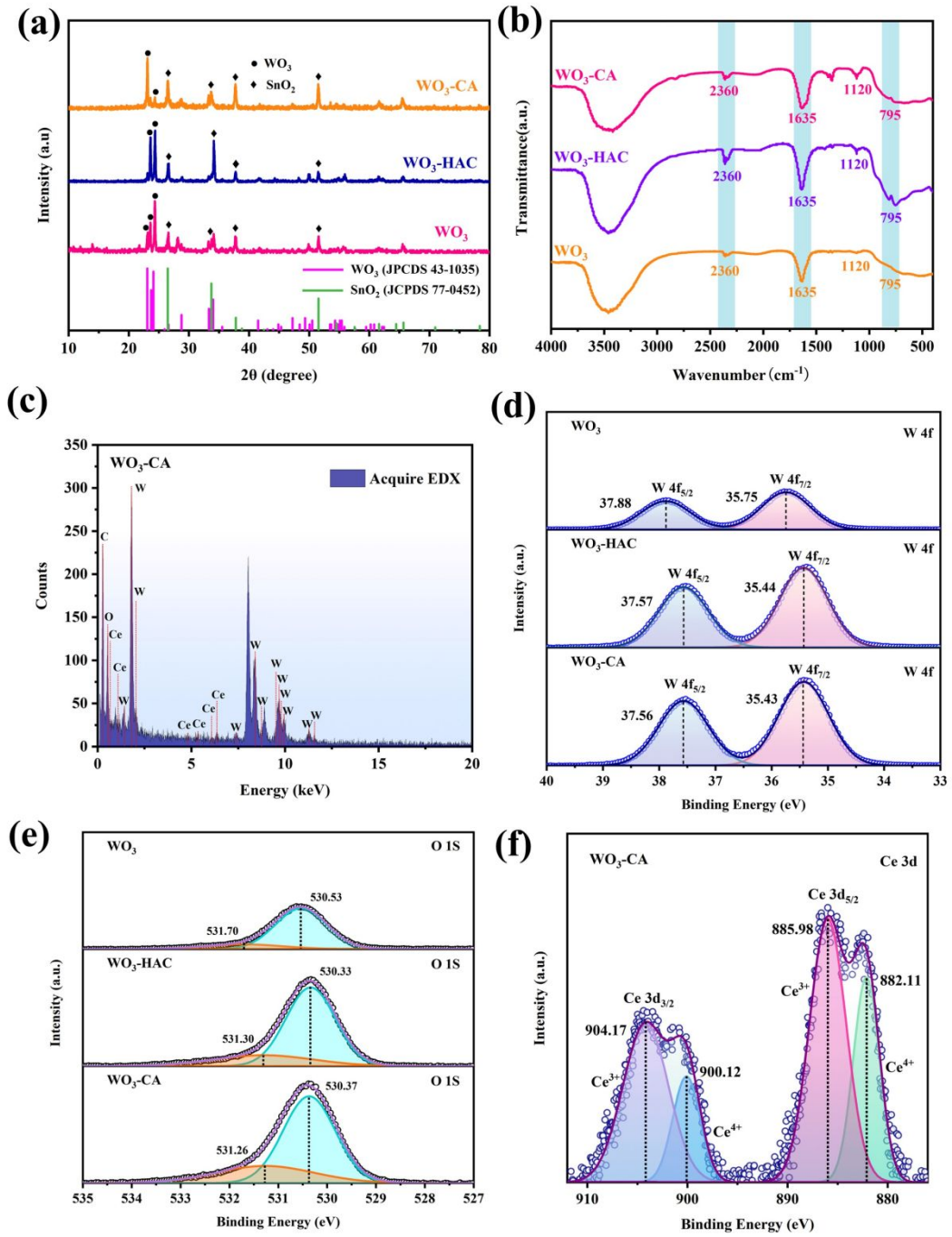

Fig. 3 (a) XRD patterns and (b) FTIR spectrum of WO_3, WO_3-HAC and WO_3-CA films. (c) EDS of W, C, O and Ce in WO_3-CA film. High-resolution (d) W 4f, (e) O 1s and (f) Ce 3d XPS spectra of WO_3, WO_3-HAC and WO_3-CA films.

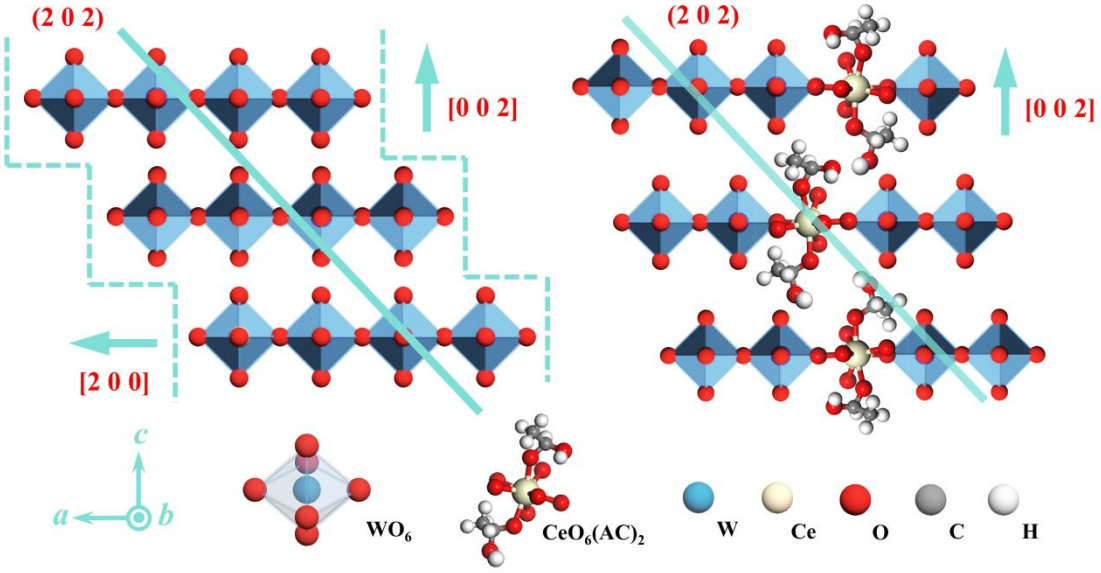

Fig. 4 Schematic diagram of the comparison mechanism between pure WO_3 films and WO_3-CA films on specific crystalline surfaces.

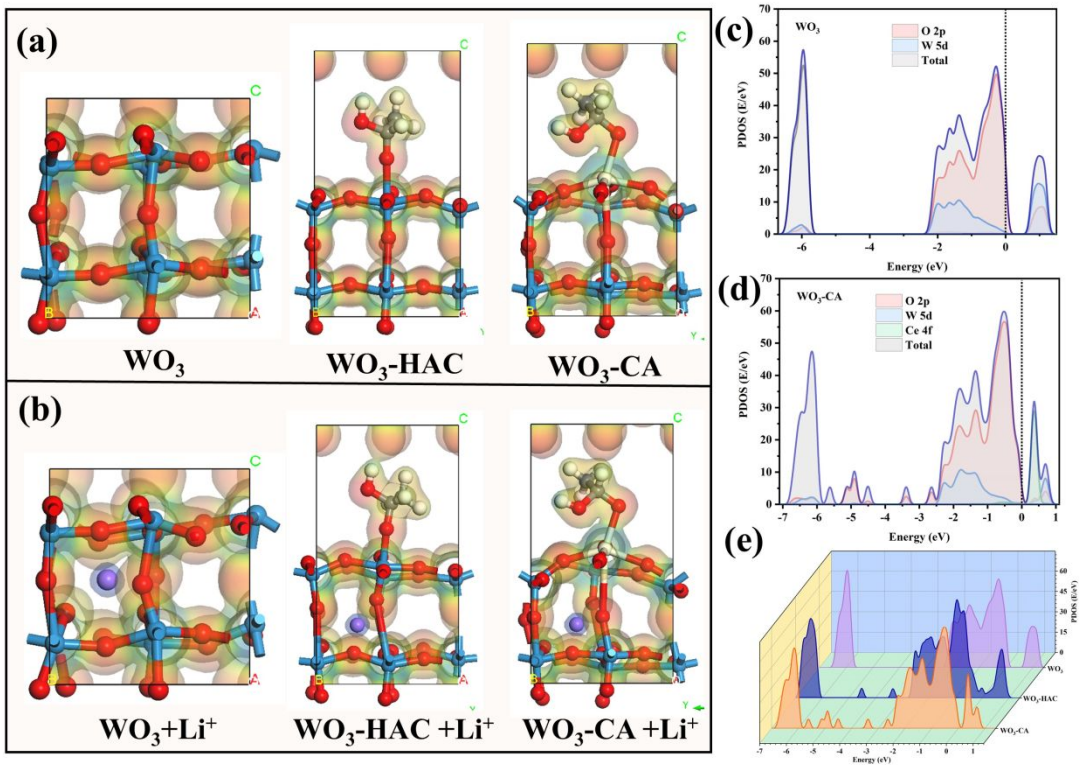

Fig. 5 (a) Computational modeling of WO_3, WO_3-HAC, and WO_3-CA and (b) corresponding charge density differences (the red and blue regions represent the accumulation and dissipation of electron density, respectively). PDOS patterns of O 2p, W 5d and Ce 4f orbitals for (c) WO_3 and (d) WO_3-CA. (e) PDOS patterns of WO_3, WO_3-HAC and WO_3-CA.

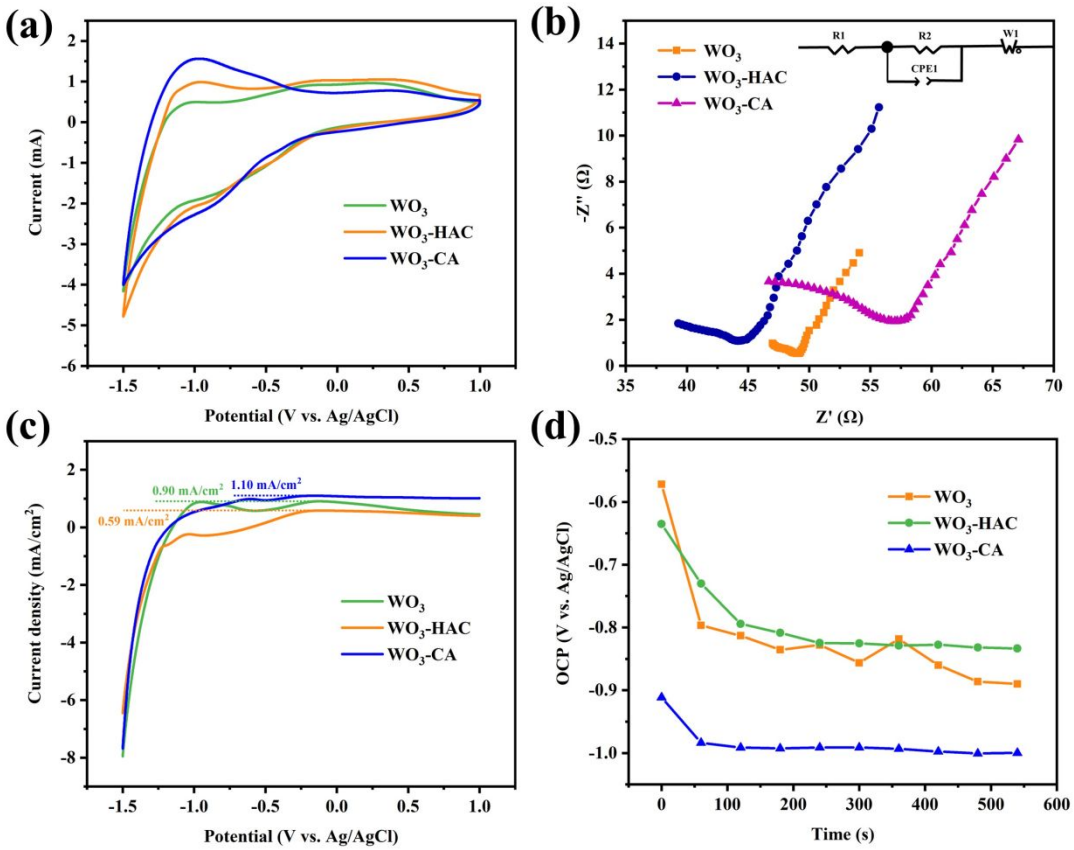

Fig. 6 WO_3, WO_3-HAC and WO_3-CA films with (a) CV curves at a scan rate of 100 mV/s, (b) EIS Nyquist plots at 0 V (V vs. Ag/AgCl), (c) I-V curves and (d) OCP curves.

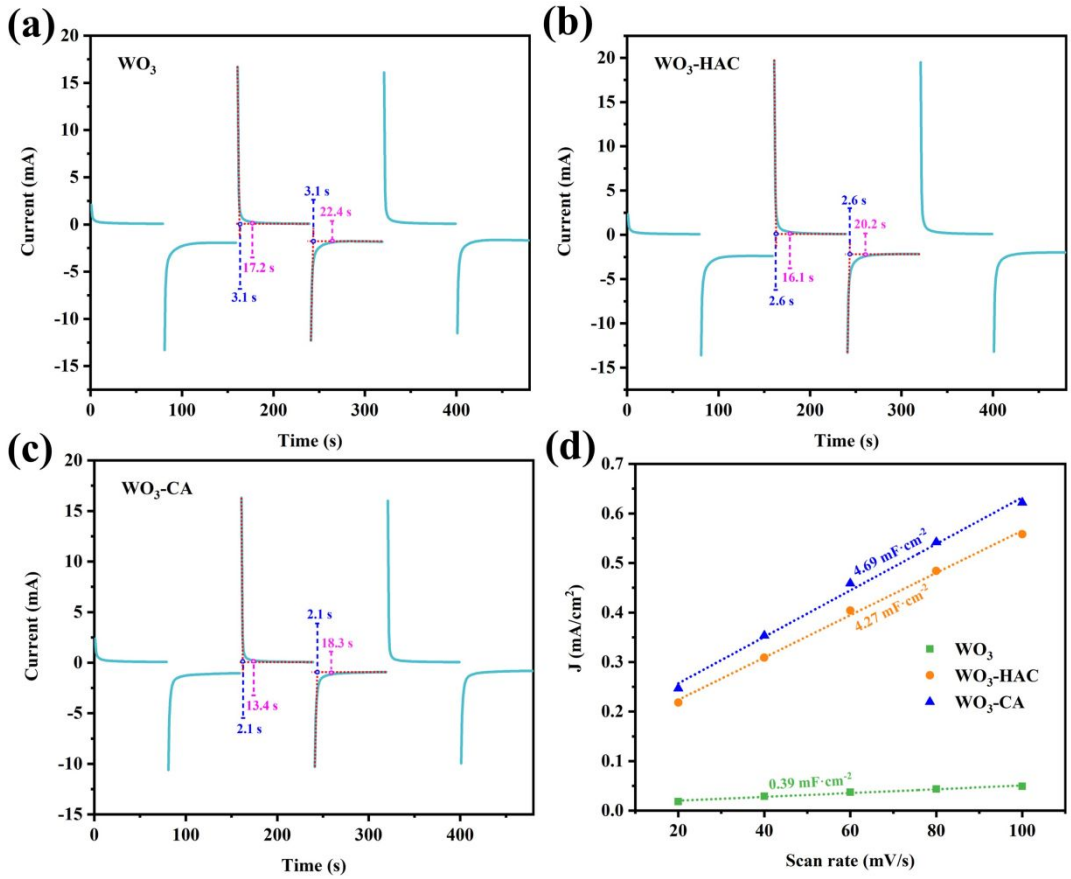

Fig. 7 Chronoamperometry measurements of (a) WO_3, (b) WO_3-HAC and (c) WO_3-CA films with a square wave potential between -1.5 V and 1.5 V (V vs. Ag/AgCl). (d) Cdl plots of WO_3, WO_3-HAC and WO_3-CA films.

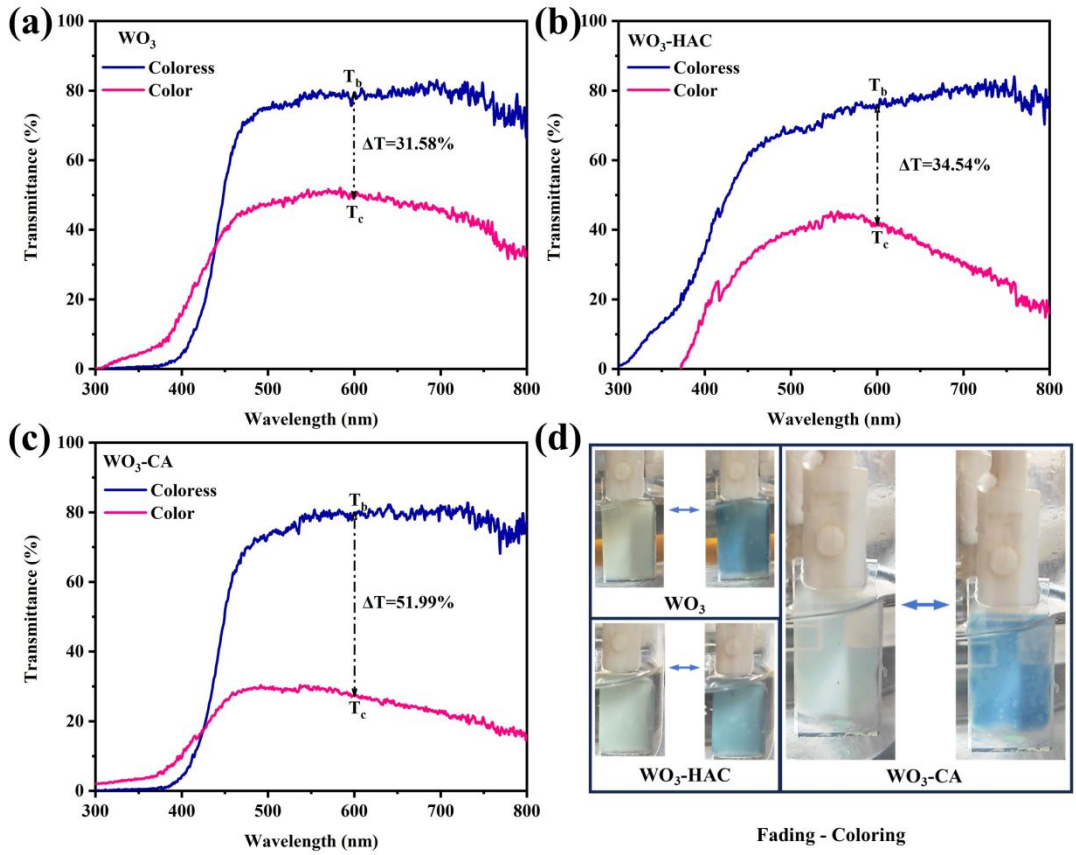

Fig. 8 Optical transmission spectra of (a) WO_3, (b) WO_3-HAC and (c) WO_3-CA films in the colored and bleached states in the range of 300 to 800 nm, and (d) corresponding color contrast plots.

Data availability statement: All relevant data are within the paper.